IJNAOE
©SNAK, 2015

Int. J. Nav. Archit. Ocean Eng. (2015) 7:559~579
http://dx.doi.org/10.1515/ijnaoe-2015-0040
pISSN: 2092-6782, eISSN: 2092-6790

An experimental study of the effect of mooring systems on the dynamics of a SPAR buoy-type floating offshore wind turbine

Sinpyo Hong[1], Inwon Lee[1], Seong Hyeon Park[2], Cheolmin Lee[2]
Ho-Hwan Chun[2] and Hee Chang Lim[3]

[1]*Global Core Research Center for Ships and Offshore Plants, Pusan National University, Busan, Korea*
[2]*Department of Naval Architecture and Ocean Engineering, Pusan National University, Busan, Korea*
[3]*School of Mechanical Engineering, Pusan National University, Busan, Korea*

Received 15 April 2014; Revised 21 January 2015; Accepted 26 March 2015

ABSTRACT: *An experimental study of the effect of mooring systems on the dynamics of a SPAR buoy-type floating offshore wind turbine is presented. The effects of the Center of Gravity (COG), mooring line spring constant, and fairlead location on the turbine's motion in response to regular waves are investigated. Experimental results show that for a typical mooring system of a SPAR buoy-type Floating Offshore Wind Turbine (FOWT), the effect of mooring systems on the dynamics of the turbine can be considered negligible. However, the pitch decreases notably as the COG increases. The COG and spring constant of the mooring line have a negligible effect on the fairlead displacement. Numerical simulation and sensitivity analysis show that the wind turbine motion and its sensitivity to changes in the mooring system and COG are very large near resonant frequencies. The test results can be used to validate numerical simulation tools for FOWTs.*

KEY WORDS: SPAR buoy; Floating offshore wind turbine; Scale model experiment; Mooring cable tension.

INTRODUCTION

Over the last several decades, renewable energy has drawn much attention due to the increasing price of fossil fuel and the increasing need for the reduction of greenhouse gas emissions. Since the oil crisis in the early 1970's, wind power technology has experienced significant development, moving from a low level experimental technology to a mainstream power technology. Currently, wind power is by far the fastest growing renewable energy source, and various wind energy generation methods have been developed.

Although global power generation from wind had reached 1.6% of the electricity generated in the world in 2010 (IEA, 2012), almost all of this generation occurred at onshore wind farms. In 2011, only 1.7% of wind energy came from offshore sources. However, offshore wind power is currently drawing considerable attention due to its advantages. One of the primary advantages is the better quality of the wind resource in sea locations, where the wind speed is usually greater, and increases with increasing distance from the coast. In addition, offshore wind is more uniform (softer). Thus, energy productivity increases and

Corresponding author: *Sinpyo Hong*, e-mail: *sinpyo@pusan.ac.kr*

wind fatigue loads on the turbine generators decrease. Another advantage comes from the larger open areas in the sea where offshore wind farms can be installed, leading to larger installations. When offshore wind turbines are located far from population areas, issues related to views and noise are eliminated, and the possibility of conflicts with coastal residents can be significantly reduced (Sheng, 2009).

In order to develop offshore wind farms, Floating Offshore Wind Turbines (FOWTs), which are applicable to deep sea locations, are being considered. FOWTs can be classified into four categories: the SPAR buoy-type, the Tension Leg Platform (TLP) type, the semi-submersible type (Lee, 2008; Jonkman, 2009), and the pontoon type. The SPAR buoy-type FOWTs considered in this study are comprised of long circular cylinders. Their stability is obtained by locating the Center of Gravity (COG) below the center of buoyancy. Their position is maintained by a combination of mooring cables and anchors. Since SPAR buoy-type FOWTs have a relatively small waterplane area, they are less affected by waves and are suitable for rough seas. At present, two commercial-scale FOWTs exist. Statoil installed a 2.3 MW SPAR buoy-type FOWT called Hywind (Neville, 2009), and Principle Power built a 2 MW semi-submersible-type FOWT called WindFloat (Rodier et al., 2010).

Many studies of FOWTs have been conducted recently (Butterfield et al., 2007; Jonkman, 2010; Jensen, 2011; Wang and Sweetman, 2012; Shin et al., 2014). The SPAR buoy-type FOWT has been studied numerically (Jonkman, 2009; Karimirad et al., 2011; Dodaran and Park, 2012; Jonkman and Musial, 2010) and experimentally using scale models (Nielsen et al., 2006; Utsunomiya et al., 2013; Goupee et al., 2012; Mostafa et al., 2012; Shin et al., 2013). However, experimental data on SPAR buoy-type FOWTs are rarely published. For research on the design of SPAR buoy-type FOWTs, more detailed and extensive experimental test results might be necessary.

An experimental study with a scale model of a SPAR buoy-type FOWT moored by springs in a wave tank is presented in this paper. The length of the scale model is about 2.5 *m*, and its scale ratio to a typical 5 MW SPAR buoy-type FOWT was taken to be 1:100. Through experiments, the effects of important floating turbine platform parameters (such as the mooring line spring constant, and the locations of the mooring fairlead and COG) on the dynamics of a SPAR buoy were investigated. Experiments with two different mooring springs, two fairlead locations, and two COGs were carried out.

To obtain useful data for the mechanical system design, nacelle acceleration and mooring line tensions were measured. A measurement system, including infrared cameras and Microelectromechanical System (MEMS) inertial sensors, was applied to obtain six Degree-of-Freedom (DOF) motion and the tension of mooring lines. The sensors attached to the scale model were small in size and light in weight, such that their effects on the model's dynamics were minimized.

Free decay and regular wave tests were conducted. In the free decay test, natural frequencies and damping coefficients of pitch and heave motions were obtained. The effect of the platform parameters, mooring line spring constant, and locations of the COG and fairlead, on the natural frequencies and damping coefficients were examined. In the regular wave test, the effects of the platform parameters on the pitch, nacelle motion, and mooring line tension were determined using Response Amplitude Operators (RAOs).

In addition to experiments, a sensitivity analysis and numerical simulations were carried out to validate the experimental results. A panel method with potential flow assumption is used for the simulations. Sensitivity analysis can provide a physical insight into the effect of system parameters on the dynamics of floating bodies. The test results from this study can be used to validate numerical simulation tools for the development of SPAR buoy-type floating offshore wind turbines.

EXPERIMENTAL SETUP

Floating body model

A scale model of SPAR buoy-type floating wind turbine was constructed. In order to compare the experimental results with the numerical calculations, a simplification of the shape of the test model and its mooring system was made so that a numerical validation for the scale model test results would be compatible. In addition, the scale model size was made as large as possible with consideration of the wave tank geometry. Figs. 1 and 2 show photographs and a simplified sketch of the floating body model, respectively. Tables 1 to 3 show some important parameters of the scale model. In the water, the draft of the scale model is about 1.2 *m*. The draft prescribed by the Offshore Code Comparison Collaboration (OC3)--Hywind of National Renewable Energy Laboratory (NREL) (Jonkman, 2010), which is a typical 5 MW SPAR buoy-type FOWT model, is 120 *m*. Therefore,

the scale ratio can be considered to be 1:100. However, the scaling of the mass and moments of inertia do not follow Froude scaling due to the simplified model shape.

In order to test the effect of the center of mass of the scale model on the platform dynamics, the model was designed with two COGs, Cg1 and Cg2. The COG can be changed with the varying platform and joint masses. Although the COG of the model changes, the total mass and center of buoyancy remain constant. However, the platform and joint have different shapes and the total yaw moment of inertia is slightly changed. Tables 2 and 3 describe the geometric parameters of the scale model--the COGs, Cg1 and Cg2, and the corresponding moments of inertia of the scale model. In the tables, Cg1 and Cg2 are measured from the bottom of the platform. Therefore, the centers of buoyancy of the model for both Cg1 and Cg2 are the same, and are located above the COGs. As a result, compared to Cg2, center of mass Cg1 has a higher value for the metacentric height, which is defined as the distance between the center of mass and metacenter.

Three catenary lines of OC3-Hywind were taken into consideration in the mooring system design of the scale model. The load-displacement relationship for surge motion of OC3-Hywind is about 40,000 *N/m* in the equilibrium state. This corresponds to 4 N/m for the surge motion of the scale model. To scale the stiffness of the catenary lines, fishing lines with stainless steel coil springs were used for the mooring system. Two different springs (with spring constants of 7.25 and 11.27 *N/m*) were used in the mooring lines. In addition, as shown in Table 1, two fairlead locations of the mooring lines were chosen near the center for L1, and at the top of the platform for L2. The fairlead location in the table is defined as the distance from the bottom of the platform to the fairlead.

A square plate on the top of the nacelle, shown in Fig. 1, was used to measure the 6-D motion of the scale model. In order to detect the motion, infrared Light-Emitting Diodes (LEDs) were attached to the plate, and a vision system with three cameras used the LEDs to measure the linear and angular displacement of the model (i.e., to detect the 6-D motion). Due to the rotationally asymmetric shape of the plate, the roll and pitch moments of inertia have different values in Tables 2 and 3.

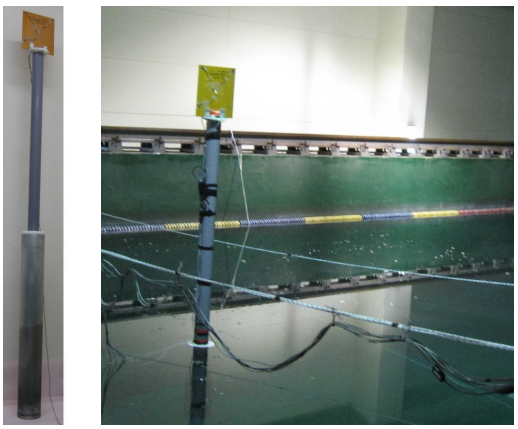

Fig. 1 Scale model figures.

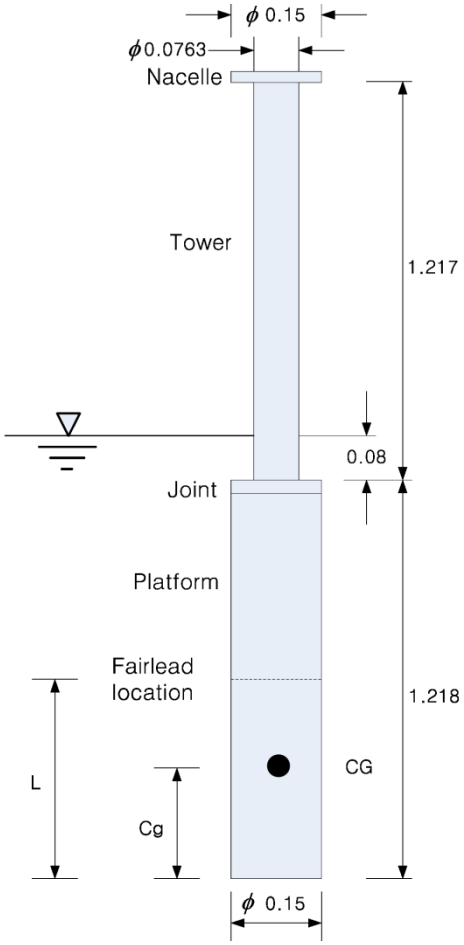

Fig. 2 Schematic view of the scale model.

Table 1 Parameters of the scale model.

Total mass		21 *kg*
Number of mooring spring		3
Spring pretension		4.8 *N*
Center of buoyancy (from the bottom of the platform)		0.620 *m*
Spring constant of each mooring spring	k1	7.25 *N/m*
	k2	11.27 *N/m*
Fairlead location (from the bottom of the platform)	L1	0.615 *m*
	L2	1.135 *m*

Table 2 Geometric parameters of the scale model for Cg1.

Center of Mass Cg1 (from the bottom of the platform)	0.448 *m*
Metacentric height	0.172 *m*
Roll moment of inertia of the whole system about Cg1	9.23735 $kg \cdot m^2$
Pitch moment of inertia of the whole system about Cg1	9.24018 $kg \cdot m^2$
Yaw moment of inertia of the whole system about Cg1	0.06466 $kg \cdot m^2$

Table 3 Geometric parameters of the scale model for Cg2.

Center of Mass Cg2 (from the bottom of the platform)	0.557 *m*
Metacentric height	0.063 *m*
Roll moment of inertia of the whole system about Cg2	9.83742 $kg \cdot m^2$
Pitch moment of inertia of the whole system about Cg2	9.84029 $kg \cdot m^2$
Yaw moment of inertia of the whole system about Cg2	0.06592 $kg \cdot m^2$

Wave tank

Fig. 3 shows the wave tank used for the model test. The tank is 100 *m* long, 8 *m* wide, and 3.5 *m* deep. The model was moored 30 *m* downstream from a wave maker, and a wave gauge was used to measure wave elevation. The vision system with three cameras and a data acquisition system was placed on the right side of the wave tank.

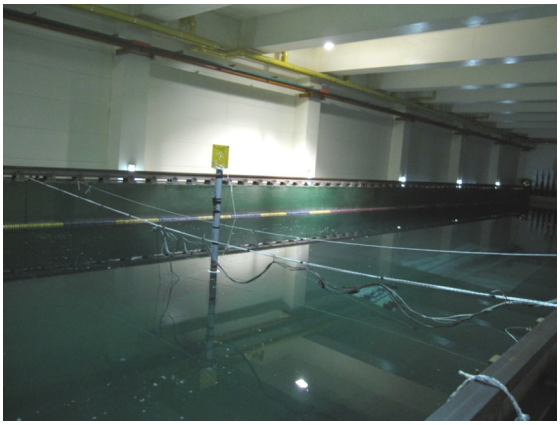

Fig. 3 Wave tank.

The configuration of the mooring system is shown in Fig. 4. The model is connected to three mooring lines with tension. Both ends of each mooring line were firmly linked to the model and to the bottom surface of the tank. In order to eliminate asymmetrical movement, one of the lines was placed toward the wave maker, and the other two lines were placed evenly apart (120°). The mooring lines were pretensioned to simulate a catenary mooring system in which the weight of the catenary mooring lines produces tension along the lines.

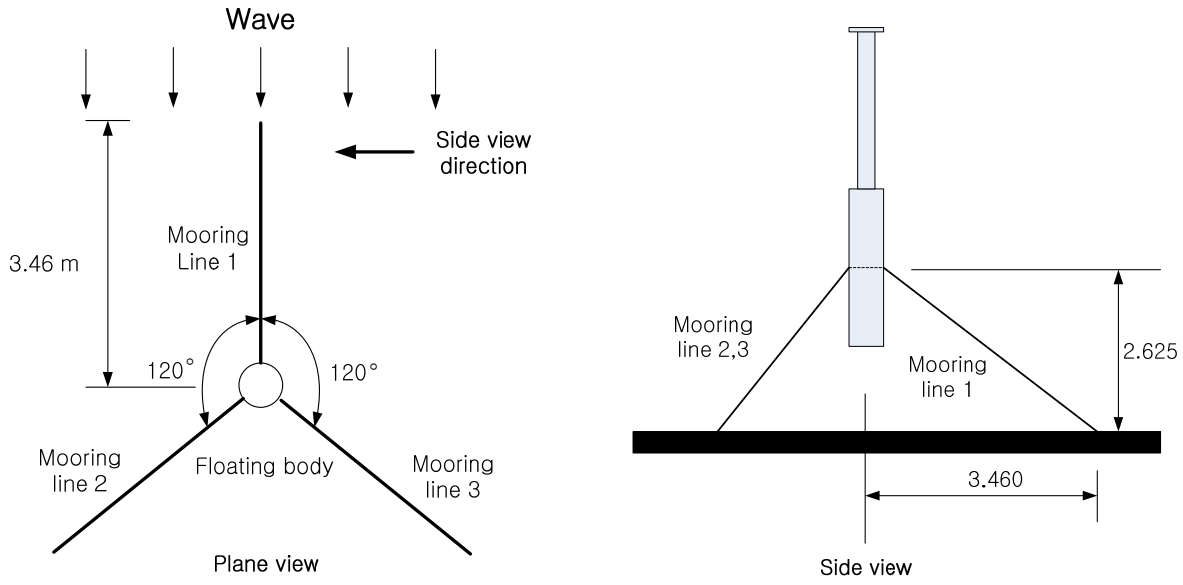

Fig. 4 Mooring system configuration in the wave tank.

Measurement system

Figs. 5 to 7 show the measurement system used for the scale model test. Fig. 5 shows the locations of sensors on the model. An Attitude Heading Reference System (AHRS) was fixed on the top of the nacelle. The AHRS contains accelerometers, gyroscopes, and magnetometers in 3-D. Its internal signal processor provides real-time 3-D orientation, 3-D acceleration, and 3-D angular rate. The sensor transmits the signal to the main computer via a Universal Serial Bus (USB) port using the RS-232 protocol.

A tension sensor and a stainless steel coil spring were inserted between the mooring line and fairlead. The tension sensors measured the amount of loaded tension occurring at the mooring lines, and the weak signals from the sensors were detected using a Wheatstone bridge. The computer acquired the signals through the bridge module. Each tension sensor is 10 *mm* in diameter and 40 *mm* in length, and weighs 10 *g*. The weight of each spring is less than 20 *g*. Since the springs and tension sensors are attached at the fairlead and their weights are very small compared with the pretension in the mooring lines, their effect on the inclined angle of the mooring lines was insignificant, and the mooring lines can be considered to be straight lines.

A 6-D camera measurement system consisting of a trinocular camera system that uses three cameras, three infrared LEDs, a camera controller, and a computer was used to measure the position and attitude of the model. The three LEDs were attached to the square plate of the scale model. The camera system, controller, and computer were placed on the right side of the wave tank. The camera measurement system measures the 3-D position and attitude of the square plate to which the LEDs were attached. The camera controller transmitted the detected signal of motion to the computer through a camera interface card so that the position and attitude of the model could be calculated in real time.

In order to measure the height of waves, a capacitive-type wave gauge was immersed in the wave tank water. The gauge signal was amplified and transmitted to the computer through an analog-to-digital converter.

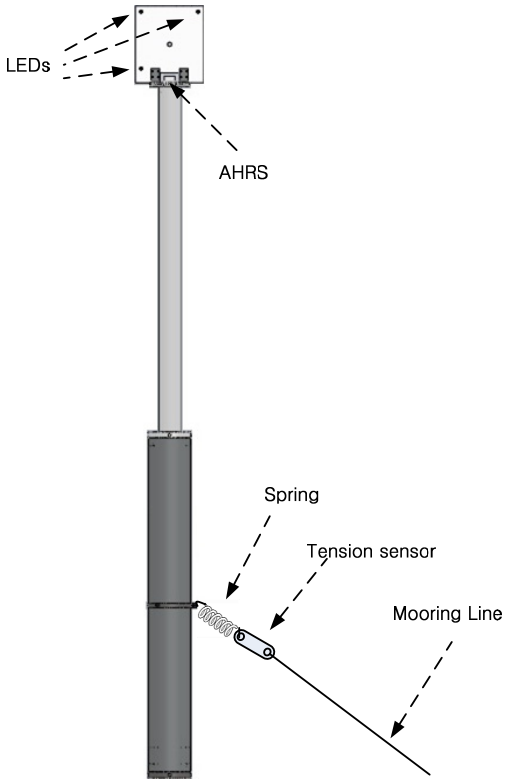

Fig. 5 Sensors located on the model.

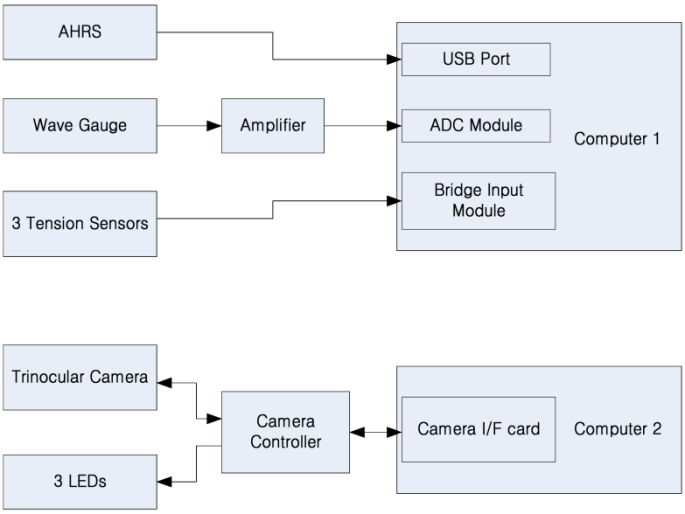

Fig. 6 Data acquisition system.

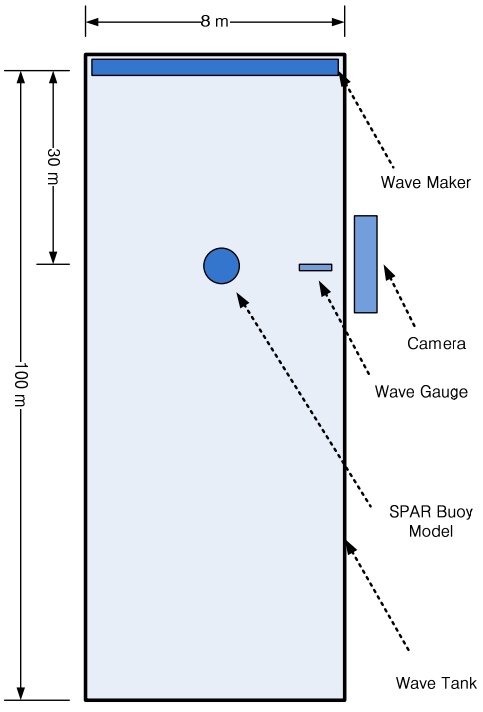

Fig. 7 Sensors equipped around the wave tank.

TEST RESULTS

The dynamic response of the scale model to water waves of small slope can be approximated with a linear second-order system with mass, damping, and stiffness components (Patel, 1989; Newman, 1977). Since the natural frequency and

damping coefficient are important parameters of a second-order system, free decay tests were conducted before the wave tests were made.

In order to find the model's natural frequencies, free decay tests were conducted without waves for different mooring spring constants, fairlead locations, and COGs. During the tests, the scale model was disturbed from its equilibrium position or attitude by applying external forces to the model. After the external force is removed, the scale model starts to oscillate around the equilibrium position and attitude with decaying amplitudes. During this transient motion period, the nacelle acceleration and angular rate from the AHRS were measured to find the natural frequencies and damping ratios. The damping ratio, ζ, is the ratio of the damping coefficient to the critical damping coefficient. Let x_1 and x_2 be the amplitudes of two successive maxima at times t_1 and t_2, respectively. The damping ratio and natural frequency ω_n can be determined from the following equations:

$$\zeta = \frac{\Delta / 2\pi}{\sqrt{1 + (\Delta / 2\pi)^2}} \tag{1}$$

$$\omega_n = \frac{\omega_d}{\sqrt{1 - \zeta^2}} \tag{2}$$

where $\Delta = \ln\left(\frac{x_1}{x_2}\right)$ and $\omega_d = \frac{2\pi}{t_2 - t_1}$.

After finding the natural frequencies and damping ratios, regular wave tests were conducted at several wave frequencies. The test wave frequencies were selected such that they are greater than natural frequencies of heave and pitch motions. The heading of wave is defined by the angle between the propagation direction and the direction from the scale model to the mooring line 1. In the wave tests, the heading is 180°; the direction of the wave is parallel to mooring line 1. During the wave tests, the tension of the mooring lines, the acceleration of the nacelle, and the pitch angle were measured for different mooring spring constants, and locations of the fairlead and COG.

Numerical simulations were performed in order to validate the experimental results. The simulation for the interaction between the wave and the FOWT model was performed using HydroStar with the panel method based on the velocity potential for time harmonic motions. For the simulation, the stiffness of the mooring system was calculated from the spring constants of the mooring lines (Patel, 1989). The results of the test and simulation are shown as Figs. 8 to 19. In the figures, test conditions for the mooring spring constant, fairlead location, and COG are given using the letters k1and k2, L1 and L2, and Cg1 and Cg2, respectively, as shown in Tables 1 to 3.

Free decay test results

Two sets of free decay tests were conducted to investigate the effect of the mooring system on the model's dynamic behavior. First, the natural frequencies and damping ratios of the model without mooring lines were obtained. Next, the mooring lines with pretension were attached to the model, and the same tests were carried out.

Figs. 8 to 10 show the variation of natural frequencies and damping ratios for various cases. In the figures, the two left columns on the graphs represent the test case in which the mooring lines are eliminated. The rest of the columns represent the case in which mooring lines are attached. Figs. 8 and 9 also compare the natural frequencies obtained from the scale model test with those from the numerical simulation.

Fig. 8 shows the variation in the natural frequency of heave motion. The graphs for Cg1, Cg2, k1L1Cg1, and k1L1Cg2 show that heave natural frequency is quite insensitive to the location of the COG. The cases for k1L1Cg1 and k2L1Cg1 show

that an increase in the mooring spring constant results in a small increase in the heave natural frequency. An interesting point to note in Fig. 8 is that the attachment of the mooring system significantly decreased the heave natural frequency. The heave natural frequencies for k1L1Cg1, k2L1Cg1, k1L2Cg1, and k1L1Cg2 are significantly lower than those for Cg1 and Cg2, which can be explained as follows.

The natural frequency of the heave motion of a moored floating system can be approximated as follows (Patel, 1989):

$$\omega_n = \sqrt{\frac{k_b + k_m}{M_b + M_a}} \tag{3}$$

$$k_b = \rho g A_w \tag{4}$$

where k_b is the spring constant of the buoyancy force, k_m is the spring constant of the mooring system, M_b is the mass of the floating system, M_a is the added mass of the floating system, ρ is the density of the fluid in which the floating system is submerged, g is the gravitational acceleration of the Earth, and A_w is the waterplane area of the floating body. Let us now consider the case in which the floating body is not attached to the mooring system. In this case, k_m is 0 and the draft is 1.188 m. As shown in Fig. 2, the waterplane passes through the platform and $A_w = \pi d_p^2 / 4$, where d_p is the diameter of the platform (0.15 *m*). Let k_{bp} denote the spring constant of the buoyancy force for this case. Then, k_{bp} is 173 *N/m*. When the mooring system is attached to the floating body with pretension, the floating body moves downward 0.11 m, and a large change in the waterplane area takes place. The waterplane passes through the tower and $A_w = \pi d_t^2 / 4$, where d_t is 0.0763 *m*. In this case, the spring constant of the buoyancy force, k_{bt}, is 44.8 *N/m*. Thus, a significant change in the spring constant of the buoyancy force occurs. Since k_m is either 10.328 *N/m* or 14.899 *N/m*, the sum of k_{bt} and k_m is much smaller than k_{bp} alone. Moreover, the attachment of the mooring system adds a small amount of mass, and the downward movement due to pretension increases the added mass by a small amount. Thus, a significant decrease in the heave natural frequency due to the attachment of a pretensioned mooring system occurs.

Fig. 9 compares pitch natural frequencies. The figure shows that the pitch natural frequency is very sensitive to the location of the COG, and less sensitive to other changes in the spring constant and fairlead location. For the model with a lower COG location, Cg1, the pitch resonant frequency is about 1.6 *rad/s*. For the model with the higher center of mass, Cg2, the pitch resonant frequency is about 0.8 *rad/s*. In addition, we note that the attachment of a mooring system increases the pitch resonant frequency by a small amount.

Fig. 10 shows damping ratios of free decay tests. Damping ratios for both the pitch and heave motions of Cg2 are higher than those of Cg1. The effect of the attachment of a mooring system on the pitch damping ratio is the opposite of the effect on the heave damping ratio: The pitch damping ratio decreases, but the heave damping ratio increases.

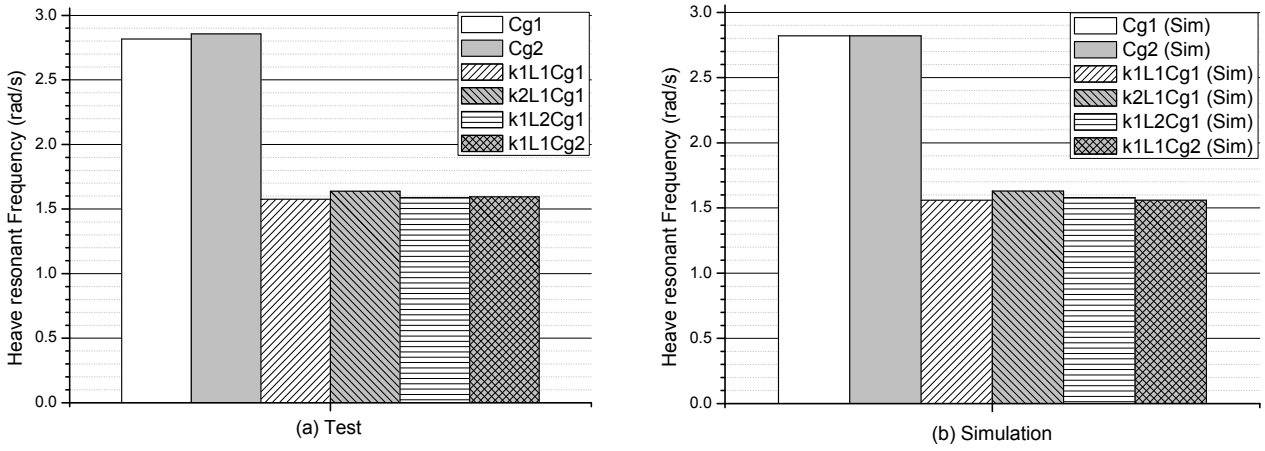

Fig. 8 Heave natural frequencies.

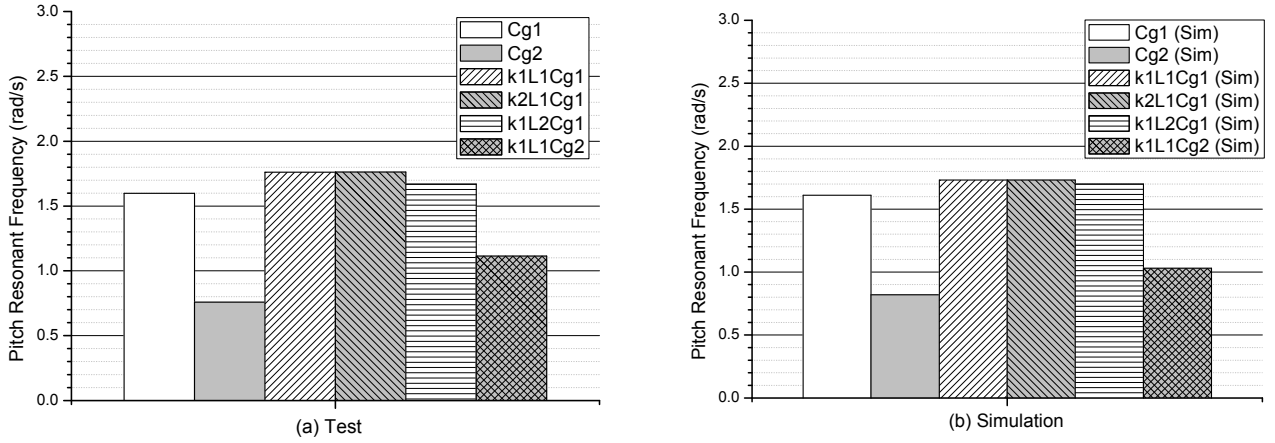

Fig. 9 Pitch natural frequencies.

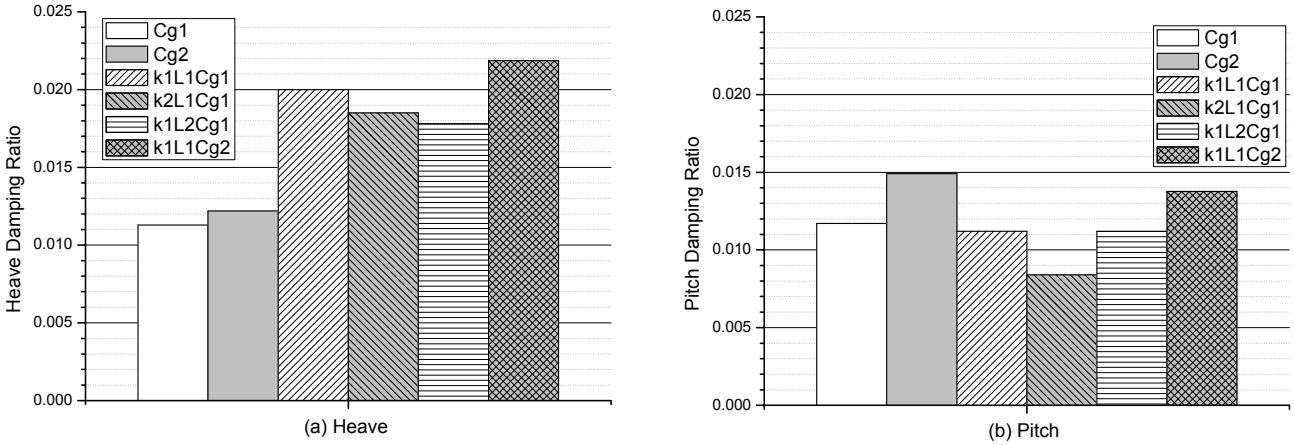

Fig. 10 Damping ratio of free decay test.

Wave test results

The natural frequencies of the model and the physical limitations of the wave maker are considered in the selection of wave frequencies. When the wave frequency is near one of the natural frequencies, the motion of the scale model becomes quite irregular, and the RAOs of the model's motion are not easy to determine. The natural frequency test results shown in Figs. 8 and 9 show that pitch and heave natural frequencies for the moored scale model are less than 2 *rad/s*. In addition, the physical characteristics of the wave maker limit the wave frequency to values of less than 1 *Hz*. Thus, the wave frequencies were selected from values between 2.5 *rad/s* and 6.3 *rad/s*. Wave heights in the tests are given in Table 4.

Figs. 11 through 19 show the results of the wave test and corresponding simulated data in terms of RAO with different mooring line spring constants, fairlead locations, and COGs. Fig. 11 shows a comparison of pitch RAOs. The RAOs increase as the wave frequency decreases. As shown in Fig. 9, the pitch natural frequencies for k1L1Cg1, k2L1Cg1, and k1L2Cg1 are about 1.8 *rad/s*. Thus, it seems reasonable that the pitch RAOs of the three test conditions increase rapidly as the wave frequency approaches the natural frequencies of the corresponding test conditions. However, the pitch RAO of k1L1Cg2 is relatively small and its slope is nearly flat. This distinctive shape could be related to the natural frequency and damping ratio of k1L1Cg2. The pitch natural frequency of k1L1Cg2 is about 1.1 *rad/s*, and is significantly smaller than those of other test conditions. Moreover, the pitch damping ratio for k1L1Cg2 is larger than those of other test conditions. These pitch RAO features are very similar to those of second-order linear systems. In the frequency response of second-order linear systems, both the amplitude and its slope decrease as the frequency increases from the resonant frequency. The amplitude of the frequency response also decreases as the damping ratio increases. Thus, the pitch RAO exhibits the dynamic characteristics of a second-order linear system.

Table 4 Wave height for regular wave tests in cm.

		Test condition			
		k1L1Cg1	k2L1Cg1	k1L2Cg1	k1L1Cg2
Wave frequency (rad/s)	2.62	3.46	3.95	2.39	3.20
	3.14	3.07	3.51	3.06	3.58
	4.19	4.16	4.57		3.45
	4.49			4.19	
	6.28	4.16	4.51	5.01	4.80

Figs. 12 and 13 show RAOs of nacelle heave acceleration and nacelle heave, respectively. The nacelle heave RAO shown in Fig. 13 was derived from the nacelle heave acceleration RAO shown in Fig. 12. The nacelle heave RAO was calculated by dividing the nacelle heave acceleration RAO by the square of the frequency. As shown in Fig. 8, the heave natural frequency of the moored scale model is about 1.6 *rad/s*. Thus, as the wave frequency approaches the heave natural frequency, the heave RAOs increase. However, heave acceleration RAOs decrease as the wave frequency approaches the heave natural frequency.

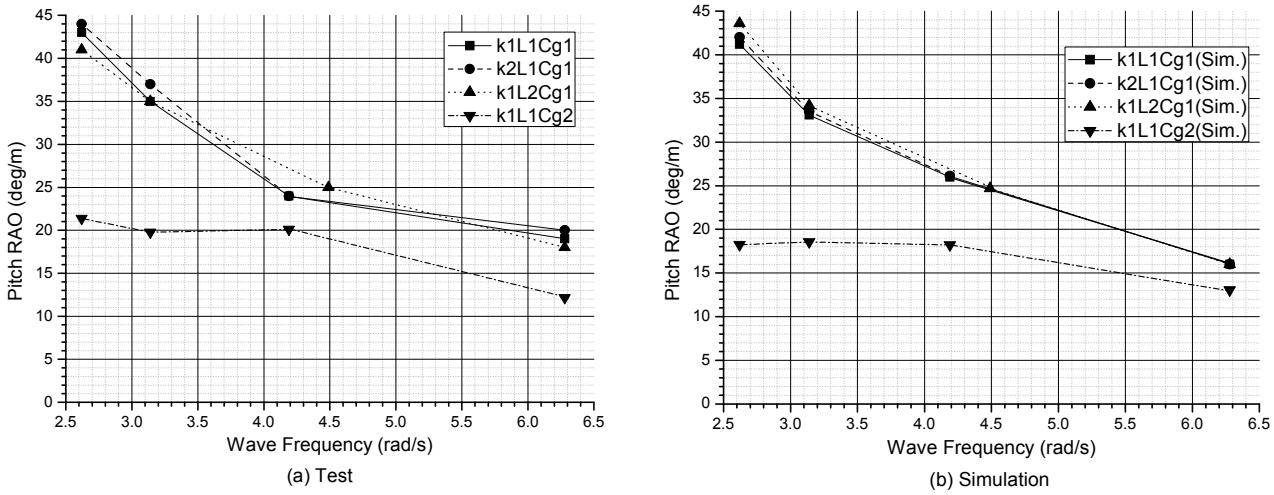

Fig. 11 Pitch RAO.

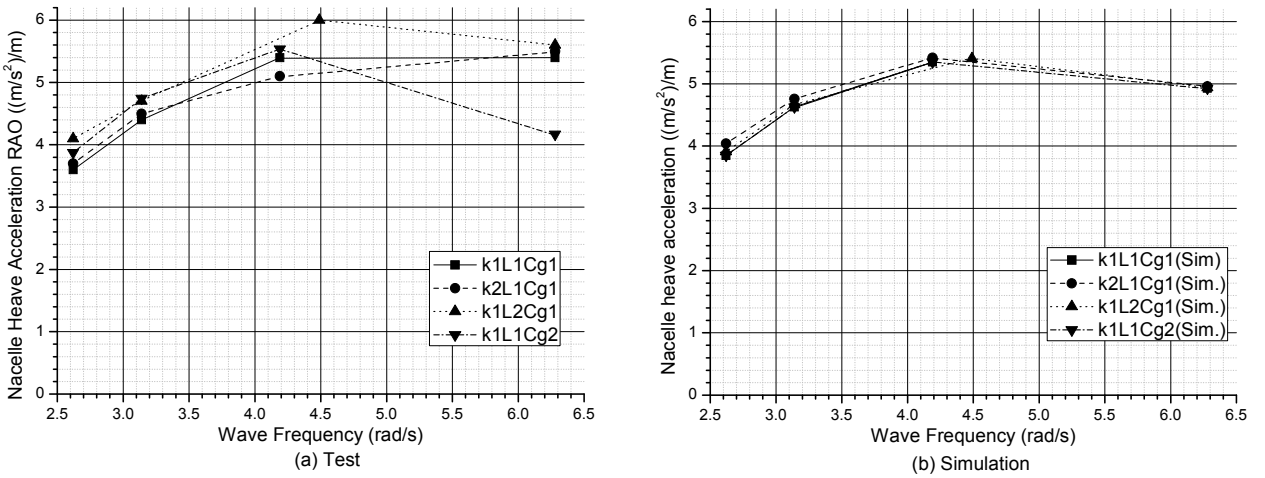

Fig. 12 Nacelle heave acceleration RAO.

Figs. 14 and 15 show nacelle surge acceleration and nacelle surge RAOs, respectively. The nacelle surge RAO given in Fig. 15 is derived from the nacelle surge acceleration RAO shown in Fig. 14 in the same way as the nacelle heave RAO. Nacelle surge displacement is a coupled motion of the surge motion of the COG and pitch motion of the scale model. Since the overall shape of the nacelle surge RAO is similar to that of the pitch RAO shown in Fig. 11, we note that pitch motion mainly contributes to the surge motion of the nacelle. As shown in Figs. 12 and 13, nacelle surge RAOs increase and nacelle surge acceleration RAOs decrease as the wave frequency approaches the pitch natural frequency.

Figs. 16 and 17 show mooring line tension RAOs. As shown in the figures for the pitch and nacelle displacement RAOs, these RAOs increase as the frequency decreases. We note that the mooring line tension RAO for k1L1Cg2 is smaller than the tensions for other test conditions. Figs. 18 and 19 show RAOs of changes in mooring line lengths. The length change of a mooring line is obtained from the tension divided by its spring constant. It is interesting to note that the length change is quite sensitive only to the fairlead location. The length change RAO for the higher fairlead location L2 is higher than that of the lower fairlead location L1. Since the mooring line length change represents the displacement of the fairlead, it can be considered that the fairlead displacement is sensitive only to the fairlead location.

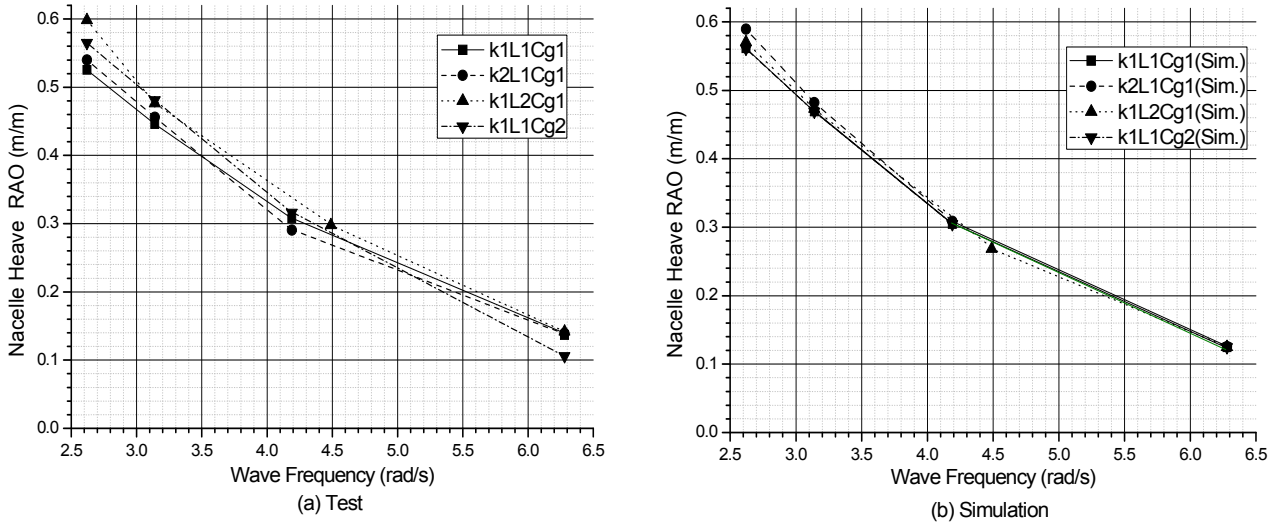

Fig. 13 Nacelle heave RAO (Nacelle heave acceleration RAO/square of wave frequency).

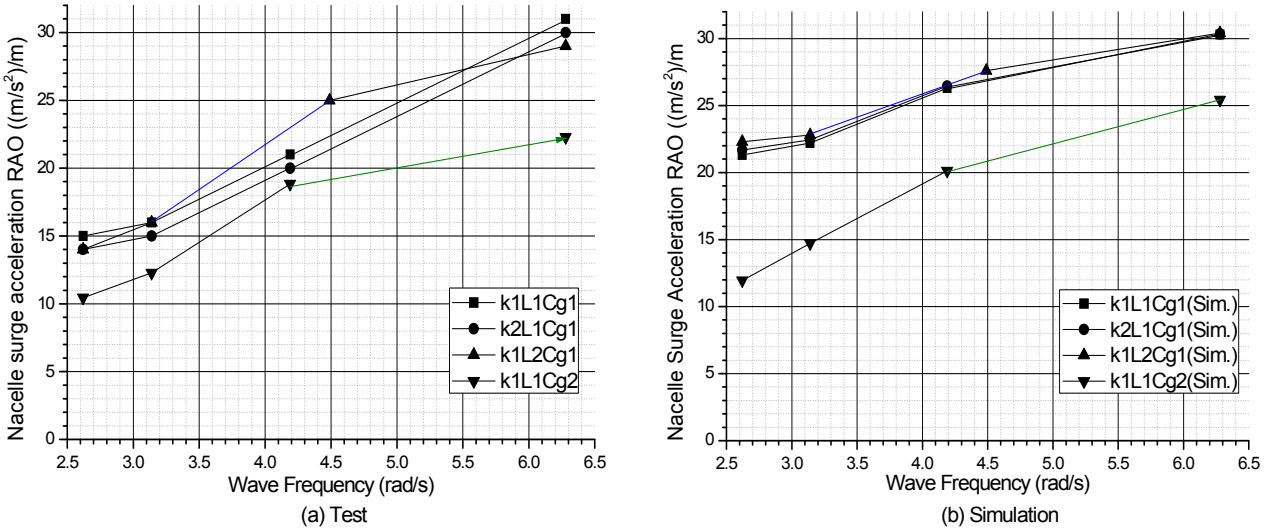

Fig. 14 Nacelle surge acceleration RAO.

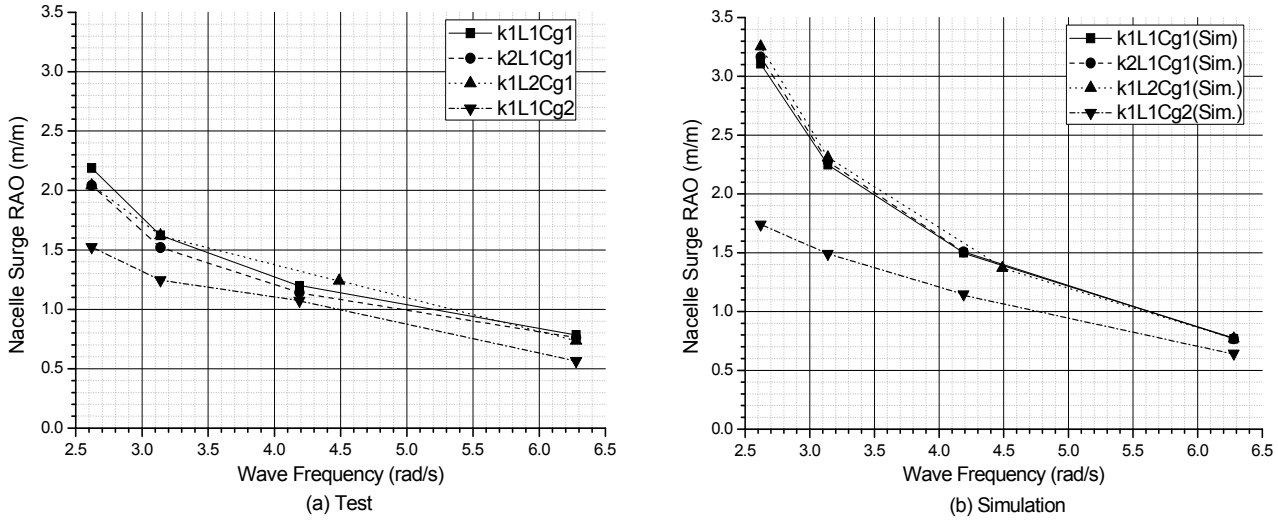

Fig. 15 Nacelle surge RAO (nacelle surge acceleration RAO/square of wave frequency).

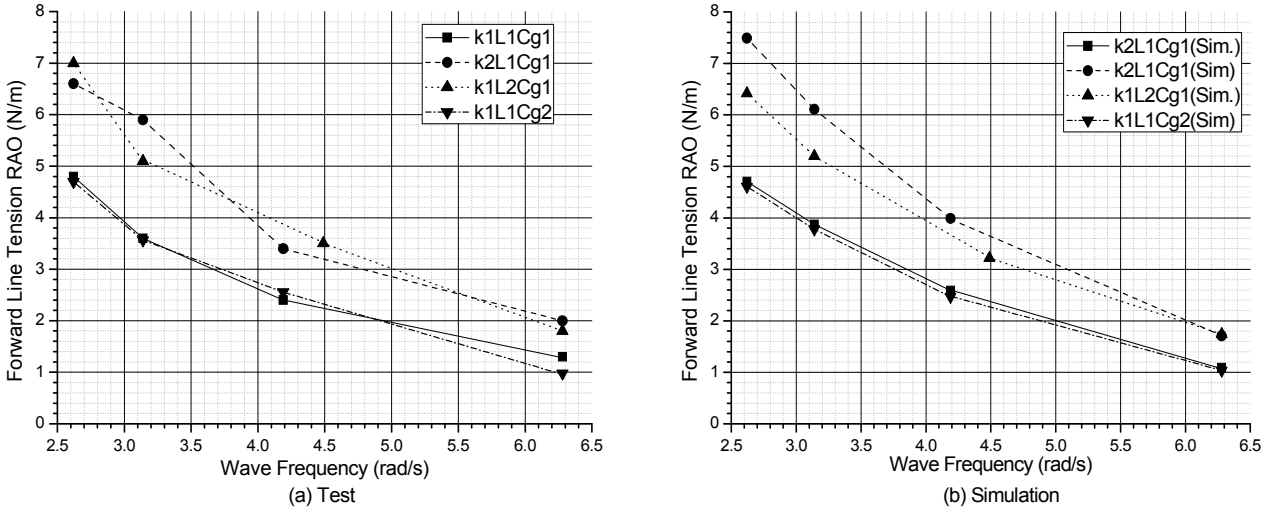

Fig. 16 Forward mooring line tension RAO.

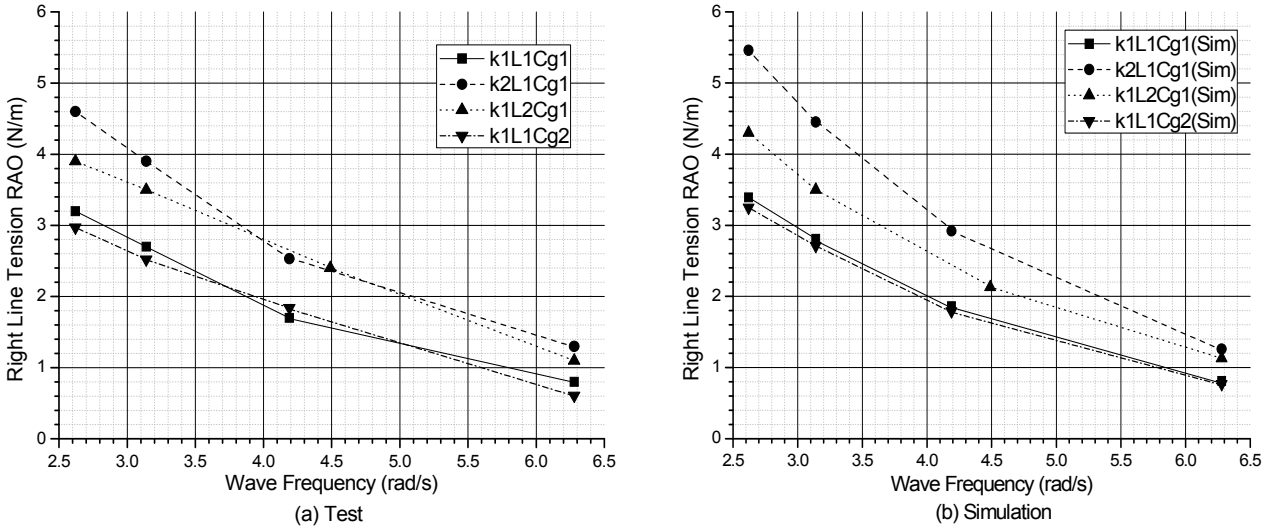

Fig. 17 Right mooring line tension RAO.

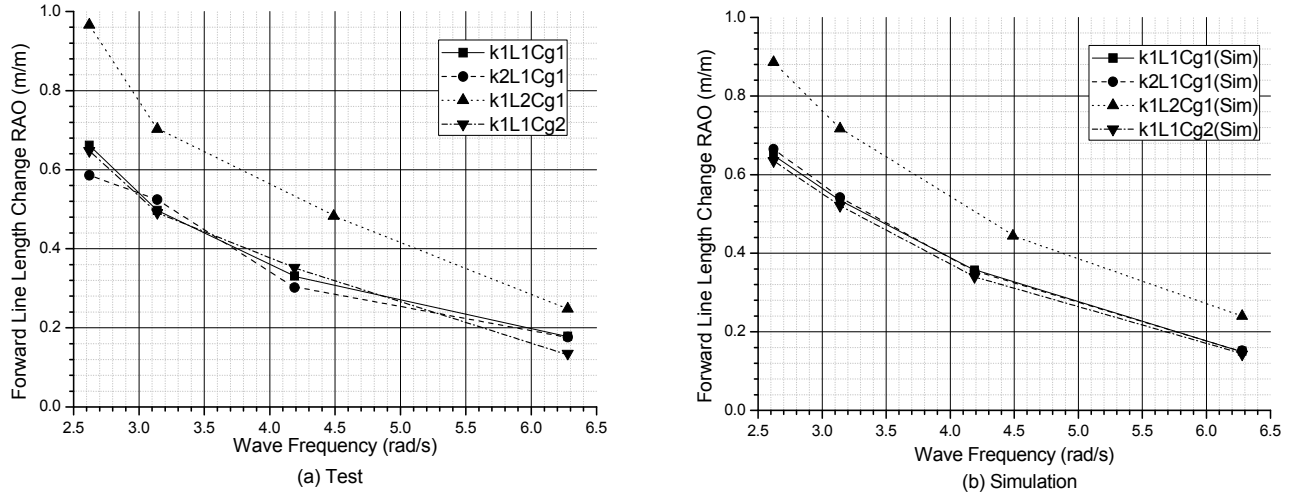

Fig. 18 Forward mooring line length change RAO.

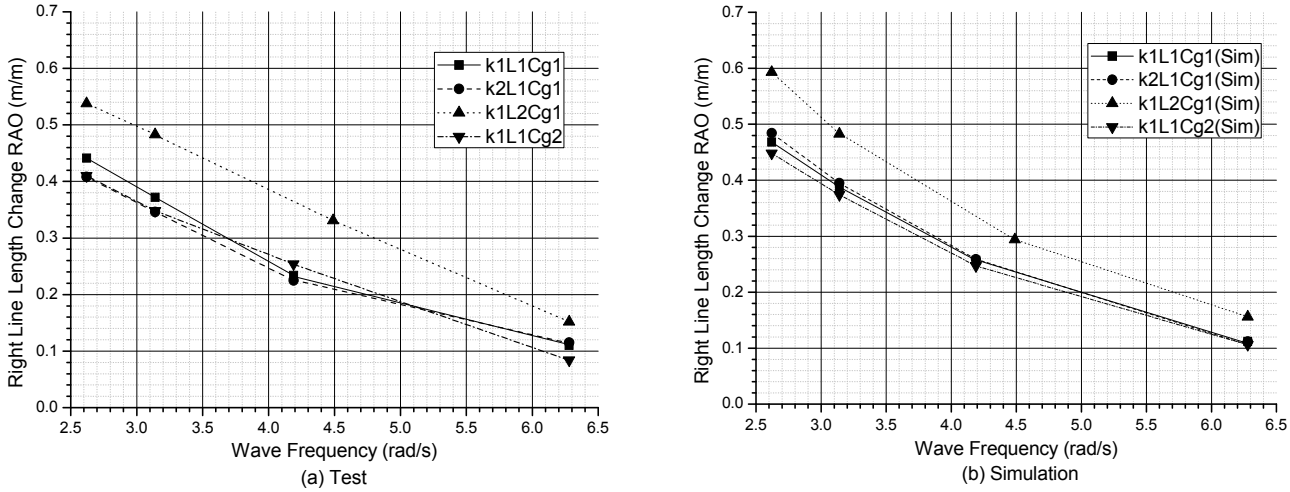

Fig. 19 Right mooring line length change RAO.

SENSITIVITY ANALYSIS

In order to understand the test results described in the previous section in a more structured way, the effects of changes in the mooring system and the COG on the scale model dynamics were analyzed using linear system theory. For a small wave slope and small body motion, the dynamics of a floating body in waves can be treated as a second-order linear system. The dynamic equations for the surge, pitch, and heave motions of the scale model with a 180° heading angle for a small wave height and negligible viscous effects can be described by the following linear second-order system (Newman, 1977):

$$\begin{bmatrix} (m_{11}+a_{11}) & a_{15} \\ a_{51} & (m_{55}+a_{55}) \end{bmatrix} \begin{bmatrix} \ddot{u}_1 \\ \ddot{u}_5 \end{bmatrix} + \begin{bmatrix} b_{11} & b_{15} \\ b_{51} & b_{55} \end{bmatrix} \begin{bmatrix} \dot{u}_1 \\ \dot{u}_5 \end{bmatrix} + \begin{bmatrix} k_{11} & k_{15} \\ k_{51} & (k_{55}+m_{11}gL) \end{bmatrix} \begin{bmatrix} u_1 \\ u_5 \end{bmatrix} = h \begin{bmatrix} F_1 \\ F_5 \end{bmatrix} \tag{5}$$

$$(m_{33}+a_{33})\ddot{u}_3 + b_{33}\dot{u}_3 + (\rho g A_w + k_{33})u_3 = hF_3 \tag{6}$$

where u_i and F_i are the ith components of the scale model motion, and the Froude-Krylov and diffraction wave forces of unit height, respectively; m_{ij}, a_{ij}, b_{ij}, and k_{ij} are the (i,j) entries of the mass, added mass, radiation damping, and the mooring

system spring constant matrices of the general six DOF motion equation, respectively; g is the gravitational acceleration, L is the metacentric height, h is the wave height, ρ is the water density, and A_w is the waterplane area of the scale model. The index numbers 1, 3, and 5 in Eqs. (5) and (6) indicate the surge, heave, and pitch motions, respectively.

For regular waves, the scale model motion and wave force can be described as

$$\begin{bmatrix} u_1 \\ u_3 \\ u_5 \end{bmatrix} = e^{j\omega t} \begin{bmatrix} \xi_1 \\ \xi_3 \\ \xi_5 \end{bmatrix}, \quad \begin{bmatrix} F_1 \\ F_3 \\ F_5 \end{bmatrix} = e^{j\omega t} \begin{bmatrix} X_1 \\ X_3 \\ X_5 \end{bmatrix} \tag{7}$$

where j is the imaginary unit, ω is the wave frequency, t is the time, and ξ_i and X_i for $i = 1, 3, 5$ are complex amplitudes. If Eq. (7) is applied to Eqs. (5) and (6), we obtain

$$\begin{bmatrix} A_{11} & A_{15} \\ A_{51} & A_{55} \end{bmatrix} \begin{bmatrix} \xi_1 \\ \xi_5 \end{bmatrix} = h \begin{bmatrix} X_1 \\ X_5 \end{bmatrix} \tag{8}$$

$$A_{33}\xi_3 = hX_3 \tag{9}$$

where

$$\begin{aligned} A_{11} &= k_{11} - (m_{11} + a_{11})\omega^2 + jb_{11}\omega \\ A_{15} &= k_{15} - a_{15}\omega^2 + jb_{15}\omega \\ A_{51} &= k_{51} - a_{51}\omega^2 + jb_{51}\omega \\ A_{55} &= k_{55} + m_{11}gL - (m_{55} + a_{55})\omega^2 + jb_{55}\omega \\ A_{33} &= k_{33} + \rho g A_w - (m_{33} + a_{33})\omega^2 + jb_{33}\omega \end{aligned} \tag{10}$$

Thus,

$$\frac{1}{h}\begin{bmatrix} \xi_1 \\ \xi_5 \end{bmatrix} = \frac{1}{A_{11}A_{55} - A_{15}A_{51}} \begin{bmatrix} A_{55} & -A_{15} \\ -A_{51} & A_{11} \end{bmatrix} \begin{bmatrix} X_1 \\ X_5 \end{bmatrix} \tag{11}$$

$$\frac{\xi_3}{h} = \frac{X_3}{A_{33}} \tag{12}$$

The RAO of ξ_i for i=1, 3, and 5 is defined as the following absolute value:

$$\left| \frac{\xi_i}{h} \right| \tag{13}$$

Since the RAOs depend on system parameters such as the mass of the scaled model, added mass, damping, and spring constants, the sensitivity of the RAO of ξ_i to a parameter p can be defined as

$$\left| \frac{\partial}{\partial p} \frac{\left|\frac{\xi_i}{h}\right|}{\left|\frac{\xi_i}{h}\right|} \right|, \; i = 1,3,5 \tag{14}$$

The RAO of the heave motion is described by a simple expression that can provide physical insights into the dynamic behavior of the scale model for changing system parameters. The heave RAO can be written as

$$\begin{aligned} \left|\frac{\xi_3}{h}\right| &= \frac{|X_3|}{\sqrt{\left[k_{33} + \rho g A_w - (m_{33} + a_{33})\omega^2\right]^2 + (b_{33}\omega)^2}} \\ &= \frac{|X_3|}{(k_{33} + \rho g A_w)\sqrt{\left(1 - \left(\frac{\omega}{\omega_{n3}}\right)^2\right)^2 + \left(2\zeta_3 \frac{\omega}{\omega_{n3}}\right)^2}} \end{aligned} \tag{15}$$

where

$$\omega_{n3} = \sqrt{\frac{k_{33} + \rho g A_w}{m_{33} + a_{33}}}, \; \zeta_3 = \frac{b_{33}}{2(m_{33} + a_{33})\omega_{n3}}, \; 0 < \zeta_3 < 1 \tag{16}$$

Even though the added masses and radiation damping are frequency dependent, the change in the sum of the scale model mass and added mass is negligible. For example, the change in $m_{33} + a_{33}$ is less than 0.4% in the frequency range of 0.3 *rad/s* to 6.28 *rad/s*. Thus, we assume that the natural frequency ω_{n3} is constant in the following sensitivity analysis for the sake of simplicity. For $\omega/\omega_{n3} >> 1$, the heave RAO can be approximated as

$$\left|\frac{\xi_3}{h}\right| \simeq \frac{|X_3|}{(k_{33} + \rho g A_w)\left(\frac{\omega}{\omega_{n3}}\right)^2} \tag{17}$$

Thus, the heave RAO does not depend on the damping ratio. For $\zeta_3 < 1/\sqrt{2}$, the heave RAO has the following maximum value:

$$\left|\frac{\xi_3}{h}\right| = \frac{|X_3|}{2(k_{33} + \rho g A_w)\zeta_3\sqrt{1 - \zeta_3^2}} \tag{18}$$

at the heave resonant frequency given by

$$\omega_{r3} = \sqrt{1 - 2\zeta_3^2}\,\omega_{n3} \tag{19}$$

Note that the peak value depends on the damping ratio. However, when $\zeta_3 > 1/\sqrt{2}$, the heave RAO does not have peaks.

The derivative of the heave RAO with respect to the mooring spring constant k_{33} is

$$\frac{\partial}{\partial k_{33}}\left|\frac{\xi_3}{h}\right| = -\frac{|X_3|\left(1-\left(\frac{\omega}{\omega_{n3}}\right)^2\right)}{\left(k_{33}+\rho g A_w\right)^2\left[\left(1-\left(\frac{\omega}{\omega_{n3}}\right)^2\right)^2+\left(2\zeta_3\frac{\omega}{\omega_{n3}}\right)^2\right]^{\frac{3}{2}}} \tag{20}$$

The sensitivity of the heave RAO to the mooring spring constant k_{33} can be written as

$$\left|\frac{\frac{\partial}{\partial k_{33}}\left|\frac{\xi_3}{h}\right|}{\left|\frac{\xi_3}{h}\right|}\right| = \frac{\left|1-\left(\frac{\omega}{\omega_{n3}}\right)^2\right|}{\left(k_{33}+\rho g A_w\right)\left[\left(1-\left(\frac{\omega}{\omega_{n3}}\right)^2\right)^2+\left(2\zeta_3\frac{\omega}{\omega_{n3}}\right)^2\right]} \tag{21}$$

For $\omega/\omega_{n3} >> 1$,

$$\left.\left|\frac{\frac{\partial}{\partial k_{33}}\left|\frac{\xi_3}{h}\right|}{\left|\frac{\xi_3}{h}\right|}\right|\right|_{\omega>>\omega_{n3}} \simeq \frac{1}{\left(k_{33}+\rho g A_w\right)\left(\frac{\omega}{\omega_{n3}}\right)^2} \tag{22}$$

Thus, the sensitivity is independent of damping ratio and decreases rapidly as the frequency ratio ω/ω_{n3} increases. As the frequency approaches zero, the sensitivity reaches a constant value such that

$$\left.\left|\frac{\frac{\partial}{\partial k_{33}}\left|\frac{\xi_3}{h}\right|}{\left|\frac{\xi_3}{h}\right|}\right|\right|_{\omega\simeq 0} \simeq \frac{1}{\left(k_{33}+\rho g A_w\right)} \tag{23}$$

Eq. (21) has a maximum value of

$$\left|\frac{\frac{\partial}{\partial k_{33}}\left|\frac{\xi_3}{h}\right|}{\left|\frac{\xi_3}{h}\right|}\right| = \frac{1}{2\zeta_3\left(1-\zeta_3\right)} \tag{24}$$

at the following frequency:

$$\omega_{p3} = \sqrt{1-2\zeta_3}\,\omega_{n3} \tag{25}$$

Note that the frequency at which the sensitivity of the heave RAO attains its maximum value, ω_{p3}, is not the same as the

resonant frequency ω_{r3}. However, as the damping ratio ζ_3 approaches zero, both ω_{r3} and ω_{p3} approach the heave natural frequency ω_{n3}, and both the heave RAO and its sensitivity to k_{33} grow rapidly.

Even though the surge and pitch dynamic responses of the scale model are coupled together and are complicated to analyze, their dynamic system equation (Eq. (5)) is basically linear, and possesses characteristics that are similar to those of heave motion with the difference that the coupled system has two resonant peaks.

In the following numerical simulation results for the sensitivity of the scale model dynamics to changes in the mooring system and the COG are given for the k1L1Cg1 test condition. HydroStar was used for the hydrodynamic calculations. The changes in the spring constant of the mooring lines and fairlead location produce changes in the system spring constants k_{11}, k_{15}, k_{51}, k_{55}, and k_{33} (Patel, 1989). A change in the COG results in changes in the metacentric height, pitch moment of inertia, and pitch load of the Froude-Kyrilov and diffraction forces. Thus, in our simulation of the sensitivity to the metacentric height, the changes in the pitch moment of inertia and pitch load of the Froude-Kyrilov and diffraction forces that are accompanied by a metacentric height change were considered. The change in the pitch moment of inertia due to the metacentric height change was calculated using Tables 2 and 3.

Fig. 20 shows RAOs of the scale model with an extended frequency range. Surge and pitch RAOs have two peaks at frequencies 0.462 *rad/s* and 1.725 *rad/s*, which are the resonant frequencies of the surge and pitch, respectively. However, the heave RAO has only one peak at the heave resonant frequency of 1.564 *rad/s*. For a frequency range that is greater than the resonant frequencies, it can be seen that the RAOs decrease as the frequency increases. However, near the resonant frequencies, the RAOs increase rapidly.

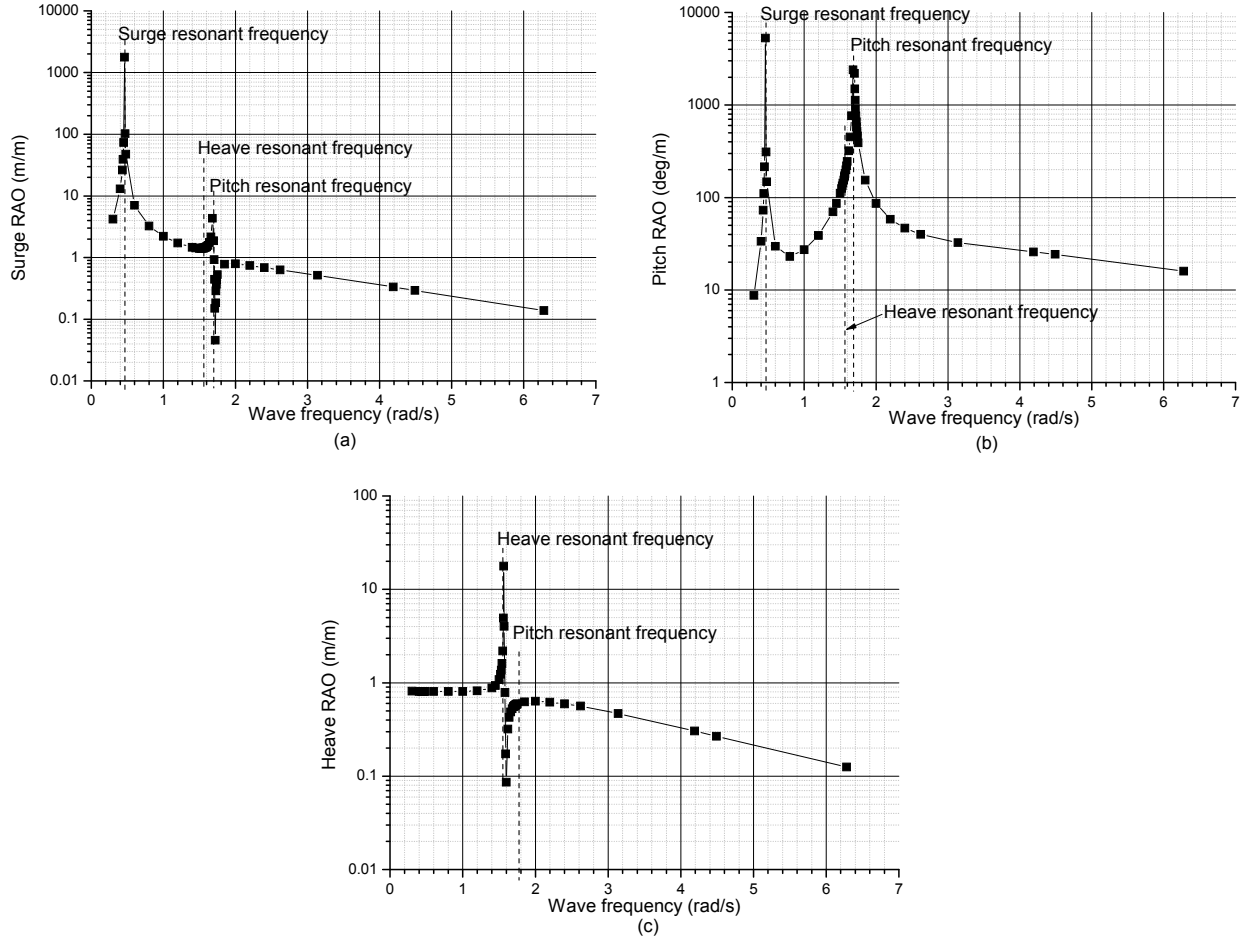

Fig. 20 RAO simulation results for k1L1Cg1 condition.

The simulation and test results of RAO sensitivities to the mooring line spring constant, fairlead location, and COG are given in Figs. 21 through 23. Since a change in COG is the same as that in metacentric height, sensitivities to COG are the same

as those to metacentric height. For the simulation, the sensitivities were calculated with small perturbations of the spring constant, fairlead location, and COG for k1L1Cg1 condition. The sensitivity test results were determined from the RAO measurements for k1L1Cg1, k2L1Cg1, k1L2Cg1, and k1L1Cg2. For example, pitch RAO sensitivity for the mooring line spring constant *k* were computed from the ratio of the difference between pitch RAO measurements for k2L1Cg1 and k1L1Cg1 to $k_2 - k_1$.

The sensitivity simulation graphs in the figures show that sensitivities near and above the resonant frequencies are quite similar to the RAOs shown in Fig. 20. For the frequency range of the scale model wave test, 2.5 *rad/s* to 6.3 *rad/s*, Fig. 21 shows that the nacelle surge and heave RAO sensitivities to the spring constants are less than 0.01 and pitch RAO sensitivity is nearly less than 0.1. Sensitivity simulation graphs in Fig. 22 show that nacelle surge and heave RAO sensitivities to the fairlead location are less than 0.1 and pitch RAO sensitivity is less than 2.0 in the wave test frequency range. However, Fig. 23 show that that nacelle surge and heave RAO sensitivities to the COG are less than 7.0 and pitch RAO sensitivity is less than 200 in the wave test frequency range.

Thus, compared to COG, the change in the mooring line spring constant has a negligible effect on the RAOs in the wave test frequency range. However, the nacelle surge and pitch RAO sensitivities to COG are noticeably large compared with those to the spring constant. The large effect of COG on the surge and pitch RAOs can be anticipated from A_{55} in Eq. (10). The derivative of A_{55} with respect to COG is $m_{11}g$. The derivative of A_{55} with respect to the spring constant is about 0.1 m^2 for k1L1Cg1 condition. Since $m_{11}g$ is greater than 200 N, the influence of the COG can be over two thousand times greater than that of the spring constant in A_{55}.

The sensitivity test graphs in the figures show that for the frequency range 2.5 *rad/s* to 4.2 *rad/s*, the test and simulation results are quite similar each other. The sensitivity differences between the test and simulation results in the higher frequency rage are considered to be caused by RAO measurement errors.

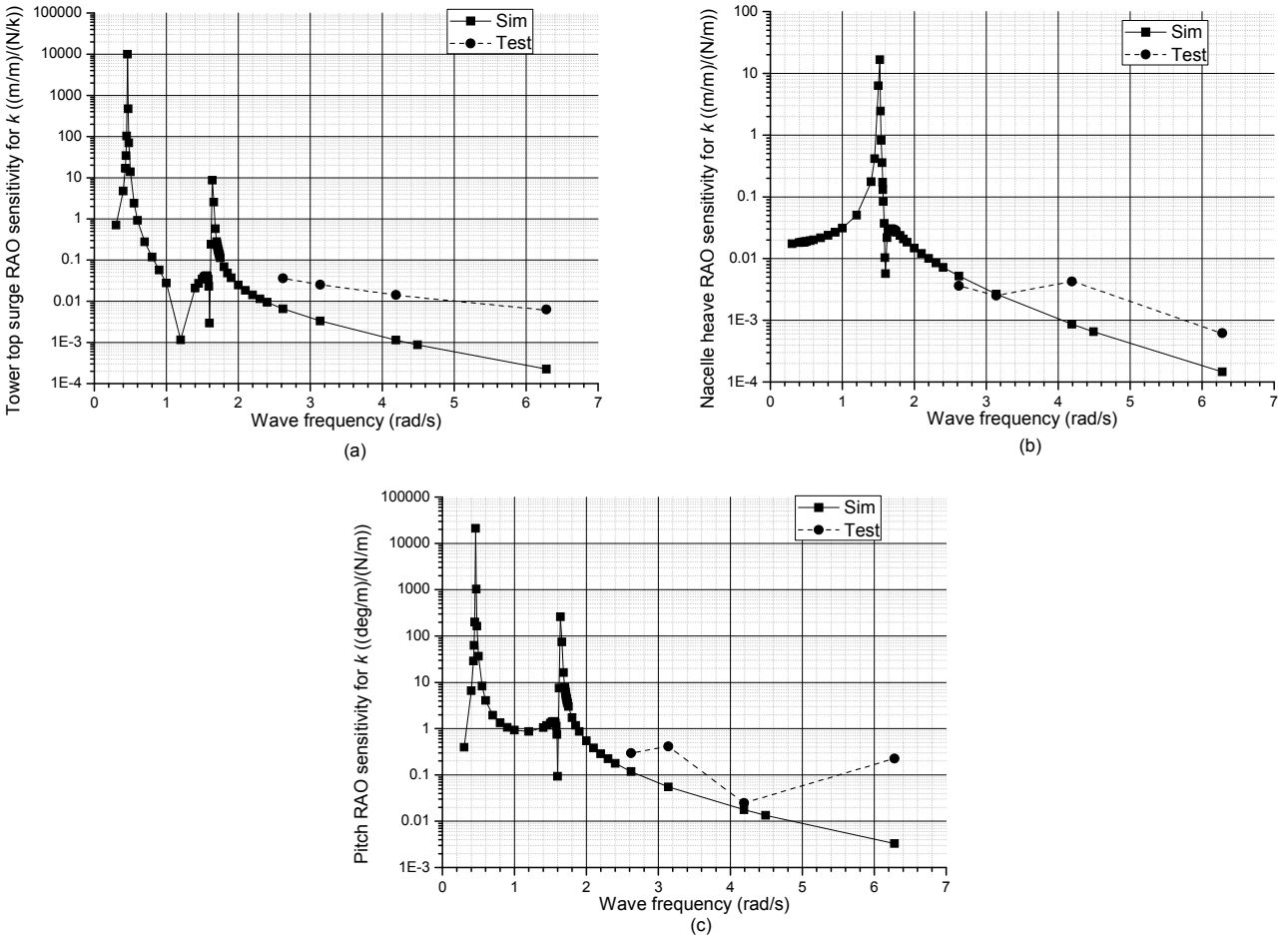

Fig. 21 Simulation and test results of RAO sensitivity for mooring line spring constant k.

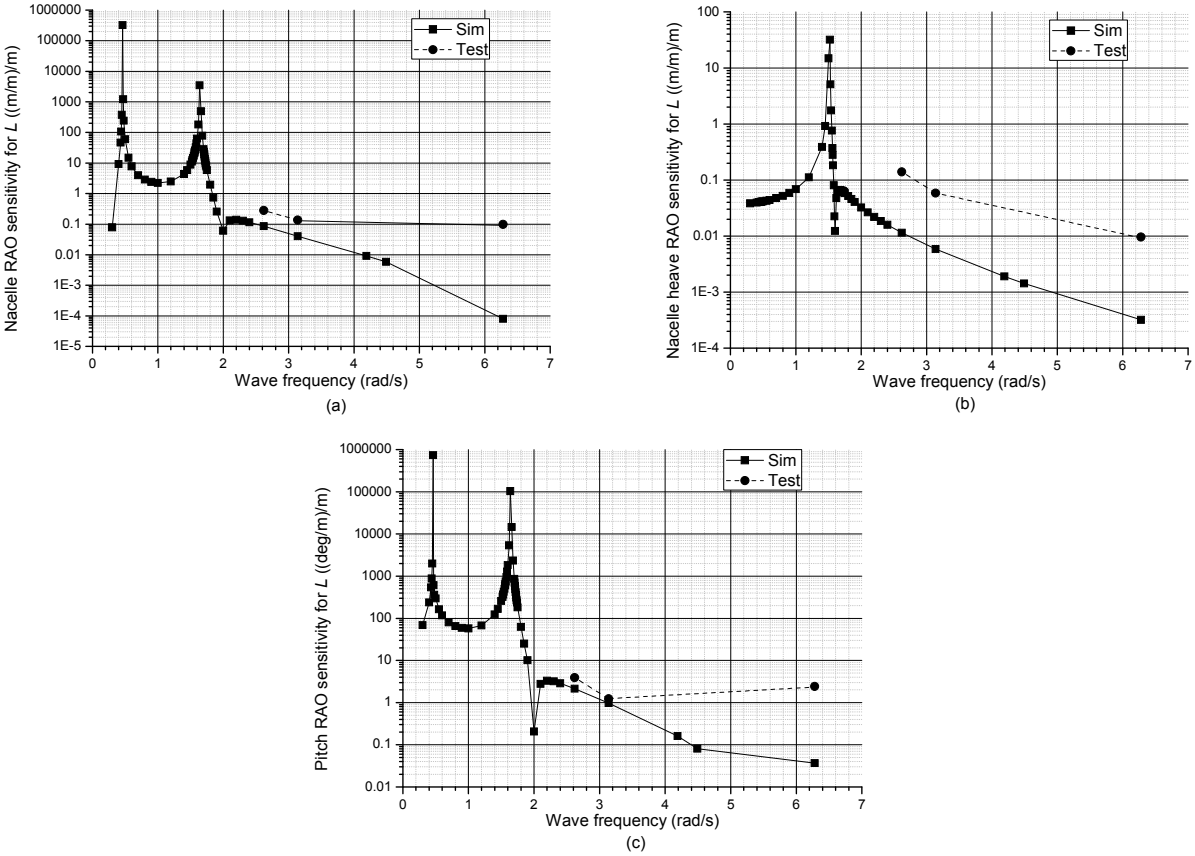

Fig. 22 Simulation and test results of RAO sensitivity for fairlead location L.

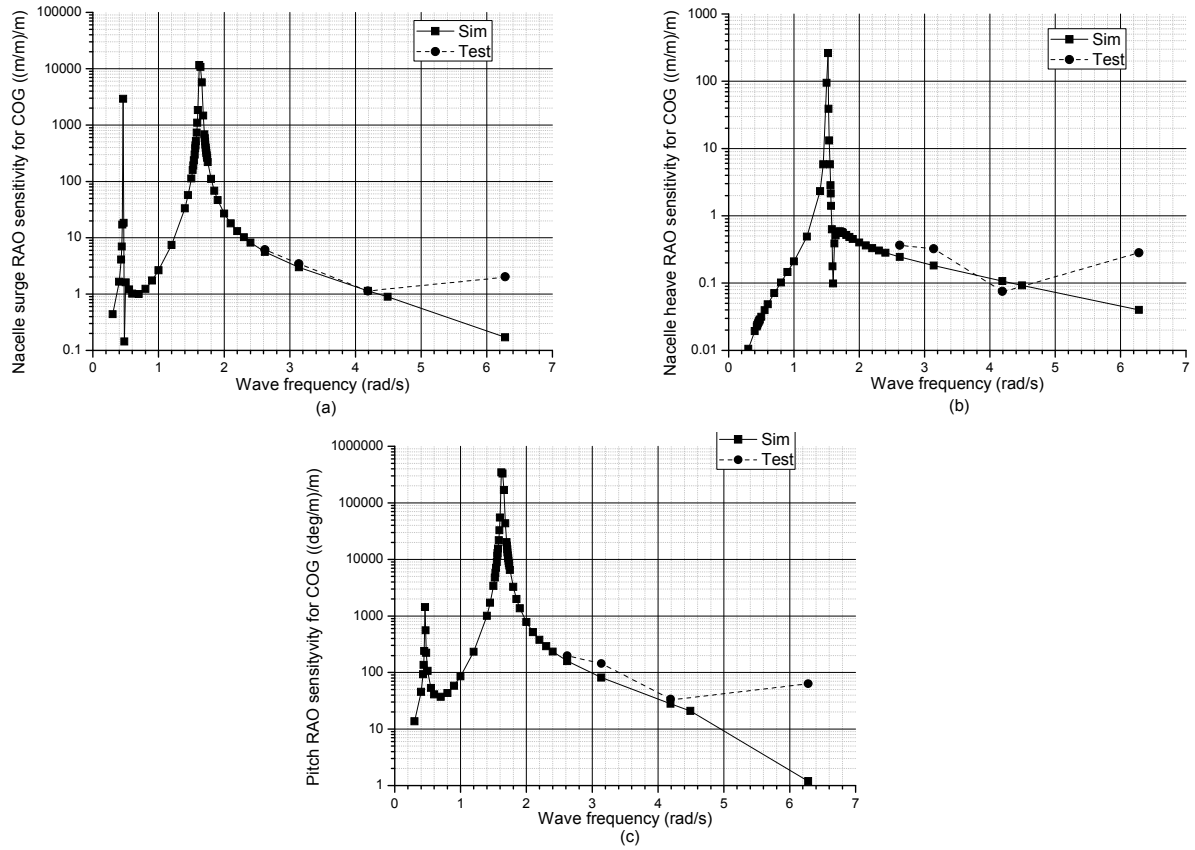

Fig. 23 Simulation and test results of RAO sensitivity for COG.

CONCLUSION

We performed an experimental study using a model of a SPAR buoy-type floating offshore wind turbine. The model was moored by springs in a wave tank, with a 1:100 scale ratio for a 5 *MW* wind turbine. Free decay and wave tests were carried out for different locations of the mooring fairlead, spring constants of mooring lines, and centers of gravity. Free decay tests for heave and pitch motions were performed to determine natural frequencies and damping ratios. Regular waves with frequencies between 1/3 *Hz* and 1 *Hz* were applied to the moored model in wave tests. The pitch, nacelle acceleration, and tensions of mooring lines were measured during the wave tests. Numerical simulations and sensitivity analyses were performed, and the results were used to validate the test results.

The free decay test results show that the heave natural frequency is very sensitive to the waterplane area, and less sensitive to changes in the mooring line spring constant, and locations of the center of gravity and fairlead. However, the pitch natural frequency is significantly affected by the location of the center of gravity. An increase in the metacentric height results in an increase in the pitch natural frequency.

Regular wave test results show that the RAOs of pitch, nacelle displacement, and mooring line tensions increase as the wave frequency decreases toward the pitch and heave natural frequencies. However, the RAO of nacelle acceleration decreases as the wave frequency decreases toward the natural frequencies.

The results also show that an increase in the height of the center of gravity produces a decrease in the pitch RAO. RAO patterns of pitch and nacelle surge are similar to each other. This implies that pitch motion mainly contributes to the nacelle surge motion.

Even though the nacelle displacement RAO has the smallest value with a high center of gravity, the RAO of the mooring line length change is mainly affected by the fairlead location. The RAO of the mooring line change increases as the height of the fairlead increases.

The test results were confirmed with numerical simulation and sensitivity analysis. It was shown that the surge and pitch motions are quite sensitive to a change in the COG. It was also shown that the platform motion, and its sensitivity to changes in the mooring system and COG, are very large near natural frequencies. The test results of the scale model described in this paper provide experimental data that can be used to validate numerical simulation tools for the development of SPAR buoy-type floating offshore wind turbines.

The scale model responses with large motion as the wave frequency approaches one of the natural frequencies in regular wave tests. Large surge or heave motion results in large changes in mooring lines and their spring constants also change. Large pitch angle breaks the linear relationship between the pitch angle and pitch moment caused by gravity. Moreover, the large oscillatory motion may produce flow separation and fluid viscosity plays an important role. Thus the model's dynamic response to wave becomes nonlinear. As a results, the model response becomes irregular and determination of RAOs can be quite confusing. Since the scale model's dynamic response around the natural frequencies is practically quite important, it can be a good research topic for future study.

ACKNOWLEDGEMENT

This work was supported by the National Research Foundation of Korea (NRF) grant funded by the Korea government (MSIP) through GCRC-SOP (No. 2011-0030013).

REFERENCES

Butterfield, S., Musial, W., Jonkman, J. and Sclavounos, P., 2007. *Engineering challenges for floating wind Turbines. Report number NREL/CP-500-38776*. Colorado: National Renewable Energy Laboratory (NREL).

Dodaran, A.A. and Park, S.K., 2012. Development of design static property analysis of mooring system caisson for offshore floating wind turbine. *International Journal of Ocean System Engineering*, 2(2), pp.97-105.

Goupee, A.J., Koo, B.J., Lambrakos, K.F. and Kimball, R.W., 2012. Model tests for three floating wind turbine concepts. *Proceedings of Offshore Technology Conference*, Houston, TX, USA, 30 April - 3 May 2012, pp.OTC 23470.

IEA, 2012. *World energy outlook 2012 – Renewable energy outlook (Chapter 7)*. Paris: International Energy Agency.

Jensen, J., Olsen, A. and Mansour, A., 2011. Extreme wave and wind response predictions. *Ocean Engineering*, 38(17-18), pp.2244-2253.

Jonkman, J., 2009. Dynamics of offshore floating wind turbines-model development and verification. *Wind Energy*, 12, pp.459-492.

Jonkman, J., 2010. *Definition of the floating system for phase IV of OC3, report number NREL/TP-500-47535*. Colorado: National Renewable Energy Laboratory (NREL).

Jonkman, J. and Musial, W., 2010. *Offshore code comparison collaboration (OC3) for IEA task 23 offshore wind technology and development, report number NREL/TP-5000-48191*. Colorado: National Renewable Energy Laboratory (NREL).

Karimirad, M., Meissonnier, Q., Gao, Z. and Moan, T., 2011. Hydro elastic code-to-code comparison for a tension leg SPAR-type floating wind turbine. *Marine Structures*, 24(4), pp.412-435.

Lee, S.H., 2008. *Dynamic response analysis of spar buoy floating wind turbine systems*. Ph.D. Thesis. MIT.

Mostafa, N., Murai, M., Nishimura, R., Fujita, O. and Nihei, Y., 2012. Study of motion of SPAR-Type floating wind turbines in waves with effect of gyro moment at inclination. *Journal of Naval Architecture and Marine Engineering*, 9, pp.67-79.

Neville, A., 2009. Hywind floating wind turbine, North Sea, Norway. *Power*, 153(12), pp.40-43.

Newman, J.N., 1977. *Marine Hydrodynamics*. Cambridge: The MIT Press.

Nielsen, F.G., Hanson, T.D. and Skaare, B., 2006. Integrated dynamic analysis of floating offshore wind turbines. *Proceedings of OMAE 2006 25th International Conference on Offshore Mechanics and Arctic Engineering*, Hamburg, 4-9 June 2006, pp.671-679.

Patel, M.H., 1989. *Dynamics of offshore structures*. London: Butterworths.

Rodier, D., Carmelli, C., Aubault, A. and Weinstin, A., 2010. WindFloat: A floating foundation for offshore wind turbines. *Journal of Renewable and Sustainable Energy*, 2, pp.033104

Sheng, J.D., 2009. Status, plans and technologies for offshore wind turbines in Europe and North America. *Renewable Energy*, 34, pp.646-654.

Shin, H., Dam, P.T., Jung, K.J., Song, J., Rim, C. and Chung, T., 2013. Model test of new floating offshore wind turbine platforms. *International Journal of Naval Architecture and Ocean Engineering*, 5(2), pp.199-209.

Shin, H., Cho, S. and Jung, K., 2014. Model test of an inverted conical cylinder floating offshore wind turbine moored by a spring-tensioned-leg. *International Journal of Naval Architecture and Ocean Engineering*, 6(1), pp.1-13.

Utsunomiya, T., Matsukuma, H., Minoura, S., Ko, K., Hamamura, H., Kobayashi, O., Sato, I., Nomoto, Y. and Yasui, K., 2013. At sea experiment of a hybrid Spar for floating offshore wind turbine using 1/10 scale model. *Journal of Offshore Mechanics and Arctic Engineering*, 135, pp.034503.

Wang, L. and Sweetman, B., 2012. Simulation of large –amplitude motion of floating wind turbines using conservation of momentum. *Ocean Engineering*, 42, pp.155-164.